crystals

MDPI

Article

Intrinsic Instability of Perovskite Solar Cells: The Role of a Hole-Blocking Layer

Nicolò Lago [1,*], Andrea Polo [1], Sathy Harshavardhan Reddy [2], Aldo Di Carlo [2] and Andrea Cester [1]

[1] Department of Information Engineering, University of Padova, 35131 Padova, Italy
[2] Department of Electronic Engineering, University of Rome "Tor Vergata", 00133 Rome, Italy
* Correspondence: lagonico@dei.unipd.it

Abstract: Among the emerging photovoltaic technologies, perovskite solar cells (PSCs) are the most promising ones with efficiencies close to crystalline silicon. However, stability and reliability issues are still a limit for future applications of this technology. This manuscript investigates the intrinsic instability of PSCs by focusing on the role of the hole-blocking layer (HBL). PSCs were fabricated employing SnO_X and bathocuproine (BCP) as an HBL, and their performances were monitored in time. The two architectures show initial similar performances; hence, they are good candidates for comparison, but they feature different instability phenomena. It is shown that cells fabricated with SnO_X present larger instabilities mainly ascribable to open-circuit voltage fluctuations (variations in the short-circuit current are negligible). In contrast, the BCP-based cells are more stable with a marginal increase in their power conversion efficiency that follows the increase in the short-circuit current (while the open-circuit voltage does not change).

Keywords: solar cells; perovskite; hole-blocking layers; tin oxide; bathocuproine

Citation: Lago, N.; Polo, A.; Reddy, S.H.; Di Carlo, A.; Cester, A. Intrinsic Instability of Perovskite Solar Cells: The Role of a Hole-Blocking Layer. *Crystals* **2023**, *13*, 185. https://doi.org/10.3390/cryst13020185

Academic Editor: Sawanta S. Mali

Received: 17 December 2022
Revised: 12 January 2023
Accepted: 18 January 2023
Published: 20 January 2023

1. Introduction

With a record efficiency above 25% [1], perovskite solar cells (PSCs) are the most interesting photovoltaic technology [2]. The combination of power conversion efficiency, which are comparable to the state-of-the-art monocrystalline silicon cells, with low-cost materials and processes makes PSCs a strategic technology with a potentiality of reaching the Shockley–Queisser limit (e.g., tandem configuration) [3].

Despite their outstanding performances, PSCs still suffer from short- and long-term instability affecting characterization reproducibility [4,5] and measurement-induce degradation [6]. In this scenario, the choice of the proper hole-blocking layer (HBL) plays a crucial role, not only to achieve high power conversion efficiencies but also to enhance the device stability [7,8].

Among several HBL materials, TiO_2 is one of the most common materials used in PSCs thanks to the proper energetic levels, allowing for the fabrication of high-efficiency cells [9,10]. However, the performance of TiO_2-based cells is still limited by the low TiO_2 n-type conductivity (electron transport layer) and the overall device stability. For this reason, alternative HBL materials were investigated [11,12]. Many alternatives have been proposed to overcome this limitation, such as doping the TiO_2 layer with Sn or Na_2S [13,14], or substituting TiO_2 with other metal oxide materials [15]. Among the others, SnO_X and BCP are two commonly adopted solutions used in substitution of TiO_2 (for a comprehensive review, the reader may refer to [16,17]). SnO_X can provide improved efficiency thanks to a higher electron mobility as well as stability by preventing perovskite contamination and phase separation [18]. Moreover, in this configuration, SnO_X can act as a barrier layer for the sputtered ITO to further improve the stability of the device [19]; whereas, bathocuproine (BCP) is used to improve a devices performance by eliminating the charge accumulation and by reducing interface recombination [20].

In this work, we analyzed SnO_X and BCP by fabricating PSCs differing only in the HBL and comparing the intrinsic stability of the devices by monitoring the cells parameters over time, which is a priority in order to understand a device's behavior during characterization and reliability studies. We observed that even though the two architectures are characterized by similar figures of merit, using BCP as a HBL allows for a larger current conversion efficiency and an improved device stability.

2. Materials and Methods

2.1. Materials

The following were use in this study: poly[bis(4-phenyl)(2,4,6-trimethylphenyl)amine] (PTAA) (Solaris Chem), [6,6]-phenyl-C61-butyric acid methyl ester (PCBM-99%-Solenne), bathocuproine (BCP-96%-Sigma-Aldrich), SnO_Xink (N31-Avantama), methylammonium bromide (MABr-99.99%-Greatcell solar), (FAI-99.99%-Greatcell solar), cesium iodide (CsI-99.99%-Sigma-Aldrich), lead bromide (PbBr2-TCI), lead iodide (PbI2-TCI), 1-butyl-3-methylimidazolium tetrafluoroborate (BMITFB-98%-ACROS), dimethylformamide (DMF-anhydrous-Sigma-Aldrich), dimethyl sulfide (DMSO-anhydrous-Sigma-Aldrich), toluene (anhydrous-Sigma-Aldrich), chlorobenzene (CB-anhydrous-Sigma-Aldrich), and dichlorobenzene (DCB-anhydrous-Sigma-Aldrich).

2.2. Devices Fabrication

Figure 1 reports the devices architecture and band diagram for both the SnO_X-based PSCs (Figure 1a,c) and the BCP-based PSCs (Figure 1b,d). The ITO/glass substrates (15 Ω/sq, 2.5 × 2.5 cm^2) were etched using a UV nanosecond laser (Spectraphysics—Andover, MA, USA). The ablation was carried out from the top side of the substrate at a repetition rate of 80 kHz, with a scanning speed of 195 mm s^{-1}. The optimal fluence per pulse (amount of energy of a single laser pulse divided for the area of the laser spot) was 280 mJ cm^{-1}. The measured insulation resistance between the subsequent photo-anodes was higher than the detection limit of our instrument (Keithley 2420, >200 MΩ), providing a full isolation. The patterned substrates were cleaned in an ultrasonic bath with a detergent solution (2% Hellmanex in deionized water) followed by deionized water, acetone, and 2-propanol, each for 15 min. After drying, they were treated for 15 min in a UV/O3 tool (Novasonic). PTAA (2 mg/mL) in toluene was spun at 5000 rpm for 30 s before being annealed at 100 °C for 10 min. After cooling, the samples were exposed to UV light for 5 min to improve the surface wettability of the PTAA. The solar cells active material is a triple cation (3C) perovskite with BMIM-BF_4 as an ionic liquid (IL) additive. The perovskite precursor with the molecular formula $Cs_{0.05}MA_{0.14}FA_{0.81}PbI_{2.7}Br_{0.3}$ (1.4M) in DMF:DMSO 3.16:1 was spin-coated at 4000 rpm for 35 s before dropping 180 µL of CB after 20 s [19,21]. The film was annealed for 10 min at 100 °C. The PCBM was spun at 1700 rpm for 30 s before being annealed at 100 °C for 5 min. The BCP (0.5 mg/mL) in isopropanol was spun at 4000 rpm for 30 s. Following that, 100 nm of Cu was evaporated defining the cell active area of 0.18 cm^2. For SnO_X-based devices, SnO_X nanoparticle dispersions (2.5 wt% suspension in butanol, acquired from Avantama AG) were filtered with a PVDF 0.45 m filter and spun at 5000 rpm for 35 s before being annealed at 120 °C for 20 min. After that, the devices were sputtered with ITO in the Kenosistic (KS400) sputtering machine with a tin-doped indium oxide target (304.8 mm × 76.2 mm, 90% In_2O_3–10% SnO_2) using a low-temperature RF magnetron sputtering with a base pressure of $5{\cdot}10^{-6}$ mbar, a working pressure of 1.1 µbar, a power density of 0.258 W·cm^{-2}, and a precursor argon flow at 40 sccm. The samples were placed onto a pallet and moved parallel to the target at a speed of 120 cm/min. Following this, 100 nm of copper was evaporated to finish the cells, which have an active area of 0.24 cm^2.

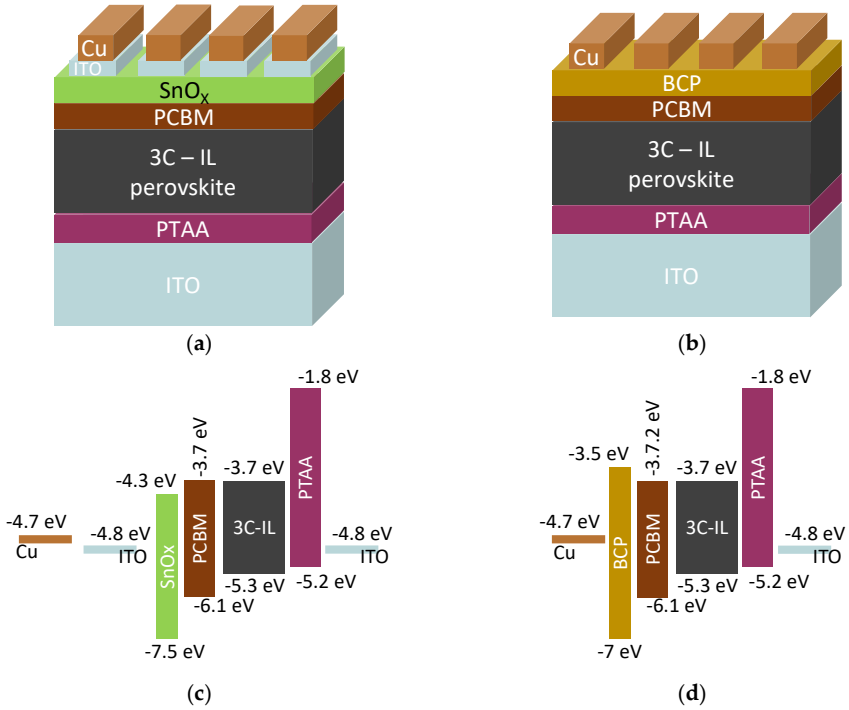

Figure 1. Architecture of the solar cells used in this work: These perovskite solar cells are based on a triple cation perovskite layer with nominal composition $Cs_{0.05}FA_{0.81}MA_{0.14}PbI_{2.7}Br_{0.3}$ along with BMIM-BF_4 ionic liquid additives, labeled as 3C-IL (**a**) SnO_X is used as a hole-blocking layer; (**b**) BCP is used as a hole-blocking layer; (**c**) and (**d**) are the qualitative band diagram for the SnO_X and BCP architectures, respectively.

To collect enough data to model the solar cells intrinsic instability, we prepared 9 SnO_X-based cells and 11 BCP-based cells. To prevent cell degradation due to the exposure of oxygen and ambient humidity, all the samples were encapsulated in a nitrogen atmosphere using a capping glass glued to the ITO/glass substrate.

2.3. Characterization Procedure

To monitor their stability over time, the cells were periodically characterized in light conditions by scanning the voltage from 0 V to 1.2 V while recording their photo-generated current. During the measurements the cells were illuminated using a white LED whose intensity was calibrated in agreement with the International Electrochemical Commission standard IEC 60904-7-2019 [22].

The cell characterization was performed in a logarithmic time scale for a total time of 10^5 s (we observed that the parameters of most of the cells stabilize within this time). The cells were kept in dark conditions between consecutive characterizations. All the experiments were performed in an ambient atmosphere at a room temperature of 23 °C.

3. Results and Discussion

In this work, we are studying two solar cell architectures differing only in the hole-blocking layer (either SnO_X or BCP). Despite sharing the same photoactive and hole-transport materials, the performance of the two architectures is visibly different.

In particular, Figure 2 reports the photo-generated current density as a function of the applied voltage for both the SnO_X architecture (blue line) and the BCP architecture (red line) measured at the beginning of the characterization procedure. As reported in Table 1, the SnO_X architecture is characterized by a larger short-circuit current J_{SC}, likely due to the large electron mobility of SnO_X (in the order of 10 to 100 $cm^2V^{-1}s^{-1}$ [23,24]; compared to 10^{-2} $cm^2V^{-1}s^{-1}$ [25] of PCBM and to 10^{-7} $cm^2V^{-1}s^{-1}$ of BCP [26]) that promotes an efficient extraction of the photo-generated electrons [27]. However, the BCP architecture

provides the highest power conversion efficiency η thanks to the larger fill-factor FF and the larger open-circuit voltage V_{OC}. It is important to notice that, among the three figures of merit (J_{SC}, FF, and V_{OC}) contributing to cell efficiency, V_{OC} is the one featuring the largest difference between the two architectures, confirming that the BCP buffer layer is beneficial in preventing interfacial recombination by reducing the voltage drop across the PCBM layer and, in turn, enhancing the built-in voltage of the device [28].

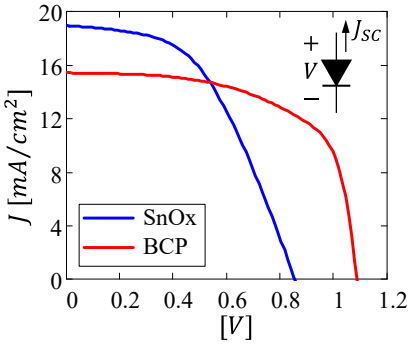

Figure 2. Illuminated current vs voltage characteristics for the SnO_X (blue line) and BCP (red line) architectures measured at the beginning of the characterization procedure.

Table 1. Solar cell figures of merit extrapolated at the beginning of the characterization procedure.

Architecture	J_{SC} [mA/cm^2]	FF [%]	V_{OC} [V]	η [%]
SnO_X	17.6 ± 1.4	51.5 ± 7.7	0.91 ± 0.05	8.4 ± 1.6
BCP	14.87 ± 0.96	63 ± 9	1.1 ± 0.02	10.5 ± 1.9

* Results are averaged over 9 samples for the SnO_X architecture, and over 11 samples for the BCP architecture. Samples active area is 0.24 cm^2 and 0.18 cm^2 for SnO_X and BCP architectures, respectively.

Another important difference between SnO_X- and BCP-based solar cells is their intrinsic instability that can be observed during subsequent characterizations over a prolonged time. However, it is important to remark that both architectures are stable during the short-term maximum power point-tracking experiment, as shown in Supplementary Figure S1.

In the following, we will analyze the figures of merit of the cells as a function of time while comparing the two architectures.

3.1. Short-Circuit Current

Figure 3 reports the normalized short-circuit current variation for the two architectures. The SnO_X-based cells feature an almost constant J_{SC} of up to 10^3 s, followed by a very small degradation (less than 0.5%). The BCP architecture instead is characterized by a much larger variability (highlighted by the wider whiskers in the box-plot chart), with a short-circuit current that increases after few seconds from the first characterization and stabilizing after 200 s with a total average increase of 5%.

In agreement with the degradation kinetics discussed by J.W. McPherson in his book [29], the J_{SC} instability for the SnO_X architecture can be described by two decaying exponentials, one to account for the degradation after 10^3 s, and one to account for the slight increase occurring at the beginning of the experiments (see the full-scale plot in Supplementary Figure S2):

$$\left.\frac{J_{SC}(t)}{J_{SC}(0)}\right|_{SnO_X} = 1 + B_1[1 - \exp(-C_1(t - t_1))]\cdot H(t - t_1) - B_2[1 - \exp(-C_2(t - t_2))]\cdot H(t - t_2), \quad (1)$$

where B_i, C_i, and t_i are empirical parameters. In particular, B_i is the magnitude of the observed instability (which can be used to predict the maximum J_{SC} variation), C_i is the exponential decay rate (which is a material dependent parameter describing the speed of

the instability), t_i is a time delay denoting the beginning of the instability process, and $H(t)$ is the step function defined as:

$$H(t - t_i) = \begin{cases} 0, & t < t_i \\ 1, & t \geq t_i \end{cases}. \quad (2)$$

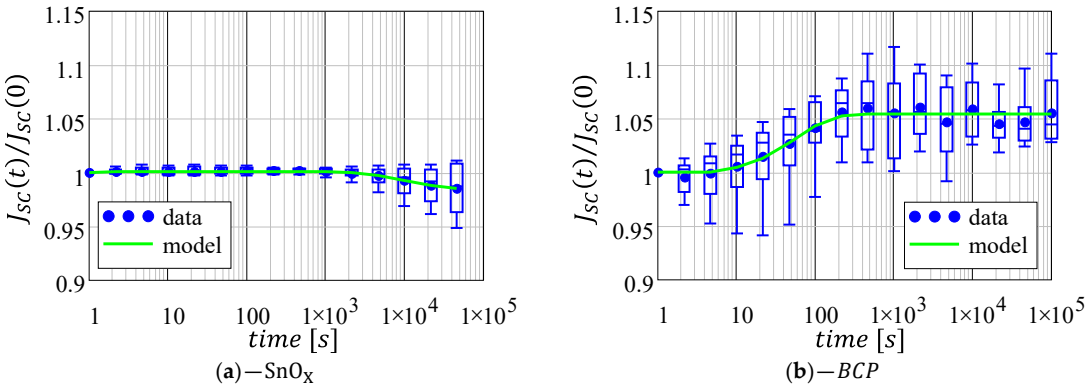

Figure 3. Normalized short-circuit current as a function of time for the two architectures under analysis: (**a**) SnO_X-based cells; (**b**) BCP-based cells. Data fitting (green line) was computed using the mean values (blue circles) as a data-set. Plots are reported with the same axis for a direct comparison. Full-scale axes are reported in Supplementary Figure S2.

In principle, Equation (1) may be used for the BCP architecture too. However, the BCP-based cells do not display any degradation during the time span of the experiments (hindering the extrapolation of parameters B_2, C_2, and t_2). Therefore, Equation (1) can be simplified by assuming $C_2 = 0\ s^{-1}$, which is the equivalent of using a single decaying exponential to describe the monotonous current increase:

$$\left.\frac{J_{SC}(t)}{J_{SC}(0)}\right|_{BCP} = 1 + B_1[1 - \exp(-C_1(t - t_1))] \cdot H(t - t_{I1}). \quad (3)$$

As reported in Figure 3, Equations (1) and (3) perfectly capture the J_{SC} behavior for the SnO_X- and the BCP-based solar cells, respectively; the corresponding fitting parameters are reported in Table 2. Notably, this model can be used to estimate the value of J_{SC} after the long-term instability of the devices are fully dissipated (i.e., $t = \infty$). For the BCP architecture, this value corresponds to parameter B_1, that in our case leads to a 5.4% increase in J_{SC}. For the SnO_X architecture, the current variation at regime can be estimated as $B_1 - B_2$, leading to a cumulative J_{SC} reduction of 1.5% with respect to its initial value. Comparing instead parameter C_1 for the two architectures, we observe that for the SnO_X-based cells C_1 is the one order of magnitude which is larger than the BCP-based cells. This indicates that, even though J_{SC} (SnO_X) displays a small variation, such variation occurs much faster in the SnO_X architecture rather that in the BCP architecture. A similar reasoning can be performed when considering the decay rate C_2, which we can assume is equal to $0\ s^{-1}$ for the BCP-based cells, suggesting that the BCP architecture is more stable than the SnO_X architecture.

Table 2. Short-circuit current fitting parameters.

Architecture	B_1 [%]	C_1 [s^{-1}]	t_1 [s]	B_2 [%]	C_2 [s^{-1}]	t_2 [s]
SnO_X	0.15	0.75	0.99	1.66	$8.1 \cdot 10^{-5}$	856.8
BCP	5.4	0.017	4.64	\	\	\

3.2. Open-Circuit Voltage

Conversely to J_{SC}, V_{OC} present the largest variability for the SnO_X architecture. Figure 4 shows the direct comparison between the SnO_X and BCP architectures, highlighting that the BCP-based solar cells are much more stable than their SnO_X counterparts, which feature V_{OC} variations of up to 100 mV when compared to an average of a few mV for the BCP architecture (see Supplementary Figure S3b).

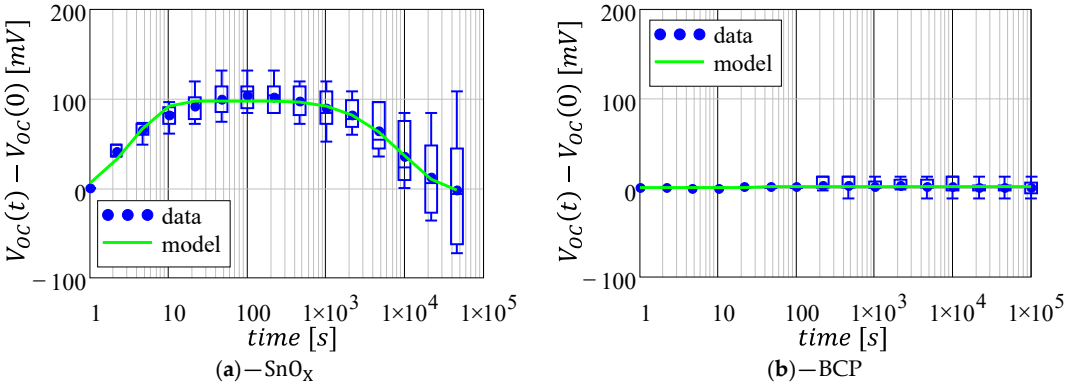

Figure 4. Normalized open-circuit voltage as a function of time for the two architectures under analysis: (**a**) SnO_X-based cells; (**b**) BCP-based cells. Data fitting (green line) was computed using the mean values (blue circles) as a data-set. Plots are reported with the same axis for a direct comparison. Full-scale axes are reported in Supplementary Figure S3.

The SnO_X architecture displays an initial improvement in the open-circuit voltage, which is followed, however, by a slow degradation that reduces the V_{OC} down to its initial value. Therefore, following the same approach used in Section 3.1, we can describe the SnO_X instability with a two-decaying exponential model, whereas a single decaying exponential can be used for the BCP instability:

$$\Delta V_{OC}(t)|_{SnO_X} = B_1[1 - \exp(-C_1(t - t_1))]\cdot H(t - t_1) - B_2[1 - \exp(-C_2(t - t_2))]\cdot H(t - t_2), \quad (4)$$

$$\Delta V_{OC}(t)|_{BCP} = B_1[1 - \exp(-C_1(t - t_1))]\cdot H(t - t_{I1}). \quad (5)$$

Table 3 shows the parameters used to fit the data in Figure 4 remarking the high stability of the BCP architecture, whereas we predict a small reduction of 2.5 mV ($B_1 - B_2$) for the SnO_X architecture after an initial variation of 100 mV (B_1). However, it is important to remark that this is an average value, and in the worst-case scenario, V_{OC} may display a degradation larger than 50 mV. The larger stability of the BCP architecture is confirmed also by the decay rate C_1, which is one order of magnitude smaller than the SnO_X cells.

Table 3. Open-circuit voltage fitting parameters.

Architecture	B_1 [mV]	C_1 [s^{-1}]	t_1 [s]	B_2 [mV]	C_2 [s^{-1}]	t_2 [s]
SnO_X	97.7	0.3	0.81	100.2	$9.6{\cdot}10^{-5}$	329.8
BCP	1.5	0.039	10	\	\	\

3.3. Fill-Factor

Figure 5 shows the variation in the fill-factor for the two architectures. Conversely to what was observed for the short-circuit current, the fill-factor for the SnO_X architecture is the one presenting the larger instability, with the FF variations within ±20% (compared to +10% for the BCP architecture). Despite this difference, for both architectures the fill-factor displays the same behavior reported for J_{SC}, even though it is much more marked in the SnO_X architecture.

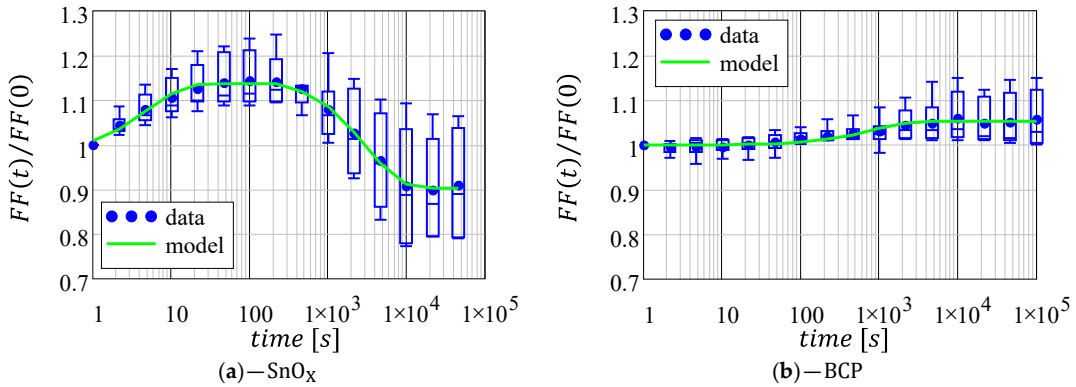

Figure 5. Normalized fill-factor as a function of time for the two architectures under analysis: (**a**) SnO_X-based cells; (**b**) BCP-based cells. Data fitting (green line) was computed using the mean values (blue circles) as a data-set. Plots are reported with the same axis for a direct comparison. Full-scale axes are reported in Supplementary Figure S4.

The SnO_X-based architecture features an initial increase in FF, followed by a degradation with respect to its initial value (around 10% degradation); whereas, the FF in the BCP architecture slightly increases and stabilizes to a +5% value.

Accordingly, the same exponential decaying models used in (1) and (3) can be used to describe the fill-factor for SnO_X- and BCP-based solar cells, respectively:

$$\left.\frac{FF(t)}{FF(0)}\right|_{SnO_X} = 1 + B_1[1 - \exp(-C_1(t - t_1))]\cdot H(t - t_1) - B_2[1 - \exp(-C_2(t - t_2))]\cdot H(t - t_2), \quad (6)$$

$$\left.\frac{FF(t)}{FF(0)}\right|_{BCP} = 1 + B_1[1 - \exp(-C_1(t - t_1))]\cdot H(t - t_{I1}). \quad (7)$$

The green lines in Figure 5 show the agreement between Equations (6) and (7) and the experimental data; whereas, the corresponding fitting parameters are summarized in Table 4. Comparing Table 2 with Table 4 we observe that for the SnO_X-based devices the decay rate (C_2) of FF is much faster than the degradation of J_{SC}; moreover, the FF reduction is twice its initial increase, leading to a final 9.7% loss of performance. Instead, for the BCP architecture J_{SC} and FF have similar magnitudes B_1 (around 5%) and similar time delays (2 and 4 s), but the FF increases with a much slower decay rate than the J_{SC} ($C_1 = 1.3{\cdot}10^{-3}$ s^{-1} compared to $17{\cdot}10^{-3}$ s^{-1}) because of the high stability in the open-circuit voltage (see Section 3.2).

Table 4. Fill-factor fitting parameters.

Architecture	B_1 [%]	C_1 [s^{-1}]	t_1 [s]	B_2 [%]	C_2 [s^{-1}]	t_2 [s]
SnO_X	13.7	0.2	0.68	23.4	$3.3{\cdot}10^{-4}$	237.5
BCP	5.2	$1.3{\cdot}10^{-3}$	2.15	\	\	\

3.4. Power Conversion Efficiency

Finally, Figure 6 reports the power conversion efficiency for the two architectures whose behavior can be predicted combining the model described in the previous subsections:

$$\eta(t)|_{SnO_X} = \left.\frac{J_{SC}(t)}{J_{SC}(0)}\right|_{SnO_X} \cdot \left.\frac{FF(t)}{FF(0)}\right|_{SnO_X} \cdot \left(1 + \left.\frac{\Delta V_{OC}(t)}{V_{OC}(0)}\right|_{SnO_X}\right), \quad (8)$$

$$\eta(t)|_{BCP} = \left.\frac{J_{SC}(t)}{J_{SC}(0)}\right|_{BCP} \cdot \left.\frac{FF(t)}{FF(0)}\right|_{BCP} \cdot \left(1 + \left.\frac{\Delta V_{OC}(t)}{V_{OC}(0)}\right|_{BCP}\right). \quad (9)$$

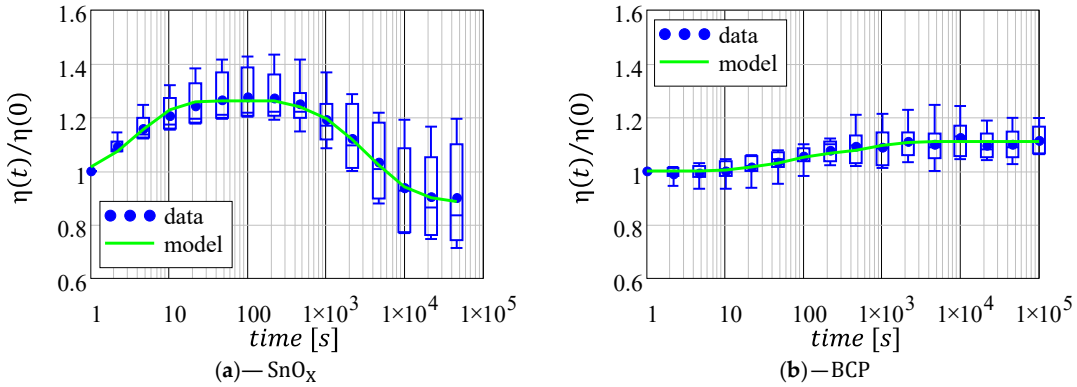

Figure 6. Normalized power conversion efficiency as a function of time for the two architectures under analysis: (**a**) SnO_X-based cells; (**b**) BCP-based cells. Data fitting (green line) was computed using the mean values (blue circles) as a data-set. Plots are reported with the same axis a direct comparison. Full-scale axes are reported in Supplementary Figure S5.

The two expressions take into account that in the previous subsections we considered the percentage variation in J_{SC} and FF normalized to the pre-test value ($t = 0$); whereas, we considered the incremental variation in V_{OC} (with respect to the pre-test value).

As expected, the efficiency reflects the instability of the previously investigated figures of merit (namely, J_{SC}, FF, and V_{OC}). In particular, the efficiency of the SnO_X cells initially increases following the increase in FF and V_{OC}, but this improvement is followed by an irreversible degradation of the overall performance as observed for all the other figures of merit (J_{SC}, FF, and V_{OC}). We believe that the commercial dispersing agents in the N31-Avantama SnO_X ink might be responsible for this degradation [19]. In contrast, the efficiency instability of the BCP-based cells is dominated by J_{SC} and FF, while V_{OC} can be assumed constant, thus a total 10% increase in efficiency is observed (5% due to the short-circuit current and 5% due to the fill-factor).

4. Conclusions

In this work, we investigated the intrinsic instability of two perovskite solar cells differing only in the hole-blocking layer (SnO_X vs BCP). The overall performance of the two architectures is similar, with SnO_X cells featuring slightly larger short-circuit currents and BCP-cells featuring slightly larger efficiency (larger V_{OC} and larger FF).

Comparing the stability of the devices, we observed two different dynamics for SnO_X- and BCP-based architectures. In particular, the SnO_X cells show an initial efficiency increase (27% increase after 100s) followed by a sensible decrease, leading to a cumulative 11% efficiency degradation. Conversely, the BCP-based cells are characterized by a monotonous increase in performance by up to 10% with respect to their initial value. Therefore, under shelf-life conditions, the BCP cells are more stable than their SnO_X counterpart; moreover, the BCP cell instability is not a detrimental phenomenon since it leads to a stable increase in performance after an initial settling time.

By analyzing separately the other figures of merit, namely J_{SC}, FF, and V_{OC}, we observed that the power efficiency instability originates mainly from one or two parameters. The SnO_X cell instability is caused mostly by V_{OC} variations, whereas the instability in the BCP-cells is observed only in J_{SC} and FF. This particular behavior suggests that to monitor PSCs, time-dependent stability is sufficient to monitor the behavior of the open-circuit voltage for SnO_X-based cells, and the behavior of the short-circuit current for the BCP-based cells.

This manuscript provides useful insights into the intrinsic instability of perovskite solar cells that are not limited to the devices used in this work. In fact, SnO_2 is currently employed for record efficacy perovskite solar cells (certified efficiency of 25.7%) [30]. Therefore, we believe that the results of this work can be an important aid to investigate degradation phenomena of high-performance solar cells.

Supplementary Materials: The following supporting information can be downloaded at: https://www.mdpi.com/article/10.3390/cryst13020185/s1, Figure S1: Maximum power point tracking; Figure S2: Normalized short-circuit current; Figure S3: Normalized open-circuit voltage; Figure S4: Normalized fill-factor; Figure S5: Normalized power conversion efficiency.

Author Contributions: Conceptualization, N.L.; methodology, N.L. and A.P.; software, N.L.; validation, N.L. and A.P.; formal analysis, N.L.; investigation, A.P.; resources, S.H.R. and A.D.C.; data curation, A.P.; writing—original draft preparation, N.L.; writing—review and editing, N.L. and S.H.R.; visualization, N.L.; supervision, A.C.; project administration, A.C. and A.D.C.; funding acquisition, A.C. and A.D.C. All authors have read and agreed to the published version of the manuscript.

Funding: This research received support from the Italian Ministry for Universities and Research through the project "Bifacial Efficient Solar cell Technology with 4 terminal architecture for Utility scale"—BEST4U (grant agreement no. ARS01_00519) and European Union's Horizon 2020 research and innovation programme under the Marie Sklodowska-Curie grant agreement no. 764787.

Data Availability Statement: The data that support the findings of this study are available on request from the corresponding author.

Conflicts of Interest: The authors declare no conflict of interest.

References

1. Best Research-Cell Efficiency Chart | Photovoltaic Research | NREL. Available online: https://www.nrel.gov/pv/cell-efficiency.html (accessed on 12 January 2023).
2. Bati, A.S.R.; Zhong, Y.L.; Burn, P.L.; Nazeeruddin, M.K.; Shaw, P.E.; Batmunkh, M. Next-Generation Applications for Integrated Perovskite Solar Cells. *Commun. Mater.* **2023**, *4*, 2. [CrossRef]
3. Kim, J.Y.; Lee, J.W.; Jung, H.S.; Shin, H.; Park, N.G. High-Efficiency Perovskite Solar Cells. *Chem. Rev.* **2020**, *120*, 7867–7918. [CrossRef] [PubMed]
4. Kang, D.H.; Park, N.G. On the Current–Voltage Hysteresis in Perovskite Solar Cells: Dependence on Perovskite Composition and Methods to Remove Hysteresis. *Adv. Mater.* **2019**, *31*, 1805214. [CrossRef] [PubMed]
5. Harshavardhan Reddy, S.; Di Giacomo, F.; Di Carlo, A.; Reddy, S.H.; Di Giacomo, F.; Di Carlo, A. Low-Temperature-Processed Stable Perovskite Solar Cells and Modules: A Comprehensive Review. *Adv. Energy Mater.* **2022**, *12*, 2103534. [CrossRef]
6. Rizzo, A.; Lamberti, F.; Buonomo, M.; Wrachien, N.; Torto, L.; Lago, N.; Sansoni, S.; Pilot, R.; Prato, M.; Michieli, N.; et al. Understanding Lead Iodide Perovskite Hysteresis and Degradation Causes by Extensive Electrical Characterization. *Sol. Energy Mater. Sol. Cells* **2019**, *189*, 43–52. [CrossRef]
7. Wang, W.; Yang, Z.; Ding, J.; Kong, J.; Li, X. Improving Water-Resistance of Inverted Flexible Perovskite Solar Cells via Tailoring the Top Electron-Selective Layers. *Sol. Energy Mater. Sol. Cells* **2022**, *238*, 111609. [CrossRef]
8. Karim, M.A.; Matsuishi, K.; Chowdhury, T.H.; Chowdhury, W.I.; Abdel-shakour, M.; Islam, A. Bathocuproine Interfacial Layer Leads to Solid Improvement of Reproducibility and Stability of Pb-Free $CsBi_3I_{10}$ Based Perovskite Solar Cells. *J. Mater. Sci. Mater. Electron.* **2022**, *33*, 8114–8126. [CrossRef]
9. Wang, P.; Shao, Z.; Ulfa, M.; Pauporté, T. Insights into the Hole Blocking Layer Effect on the Perovskite Solar Cell Performance and Impedance Response. *J. Phys. Chem. C* **2017**, *121*, 9131–9141. [CrossRef]
10. Gagliardi, S.; Rondino, F.; Paoletti, C.; Falconieri, M. On the Morphology of Nanostructured TiO_2 for Energy Applications: The Shape of the Ubiquitous Nanomaterial. *Nanomaterials* **2022**, *12*, 2608. [CrossRef]
11. Zhang, T.; He, Q.; Yu, J.; Chen, A.; Zhang, Z.; Pan, J. Recent Progress in Improving Strategies of Inorganic Electron Transport Layers for Perovskite Solar Cells. *Nano Energy* **2022**, *104*, 107918. [CrossRef]
12. Yates, H.M.; Afzaal, M.; Walter, A.; Hodgkinson, J.L.; Moon, S.J.; Sacchetto, D.; Bräuninger, M.; Niesen, B.; Nicolay, S.; McCarthy, M.; et al. Progression towards High Efficiency Perovskite Solar Cells via Optimisation of the Front Electrode and Blocking Layer. *J. Mater. Chem. C* **2016**, *4*, 11269–11277. [CrossRef]
13. Chen, S.H.; Ho, C.M.; Chang, Y.H.; Lee, K.M.; Wu, M.C. Efficient Perovskite Solar Cells with Low J-V Hysteretic Behavior Based on Mesoporous Sn-Doped TiO_2 Electron Extraction Layer. *Chem. Eng. J.* **2022**, *445*, 136761. [CrossRef]
14. Sun, H.; Xie, D.; Song, Z.; Liang, C.; Xu, L.; Qu, X.; Yao, Y.; Li, D.; Zhai, H.; Zheng, K.; et al. Interface Defects Passivation and Conductivity Improvement in Planar Perovskite Solar Cells Using Na_2S-Doped Compact TiO_2 Electron Transport Layers. *ACS Appl. Mater. Interfaces* **2020**, *12*, 22853–22861. [CrossRef]
15. Cao, Z.; Li, C.; Deng, X.; Wang, S.; Yuan, Y.; Chen, Y.; Wang, Z.; Liu, Y.; Ding, L.; Hao, F. Metal Oxide Alternatives for Efficient Electron Transport in Perovskite Solar Cells: Beyond TiO_2 and SnO_2. *J. Mater. Chem. A* **2020**, *8*, 19768–19787. [CrossRef]
16. Jiang, Q.; Zhang, X.; You, J.; Jiang, Q.; Zhang, X.; You, J. SnO_2: A Wonderful Electron Transport Layer for Perovskite Solar Cells. *Small* **2018**, *14*, 1801154. [CrossRef]
17. Ferguson, V.; Silva, S.R.P.; Zhang, W. Carbon Materials in Perovskite Solar Cells: Prospects and Future Challenges. *Energy Environ. Mater.* **2019**, *2*, 107–118. [CrossRef]

18. Xiong, L.; Guo, Y.; Wen, J.; Liu, H.; Yang, G.; Qin, P.; Fang, G.; Xiong, L.B.; Guo, Y.X.; Liu, H.R.; et al. Review on the Application of SnO_2 in Perovskite Solar Cells. *Adv. Funct. Mater.* **2018**, *28*, 1802757. [CrossRef]
19. Reddy, S.H.; Di Giacomo, F.; Matteocci, F.; Castriotta, L.A.; Di Carlo, A. Holistic Approach toward a Damage-Less Sputtered Indium Tin Oxide Barrier Layer for High-Stability Inverted Perovskite Solar Cells and Modules. *ACS Appl. Mater. Interfaces* **2022**, *14*, 51438–51448. [CrossRef]
20. Chen, C.; Zhang, S.; Wu, S.; Zhang, W.; Zhu, H.; Xiong, Z.; Zhang, Y.; Chen, W. Effect of BCP Buffer Layer on Eliminating Charge Accumulation for High Performance of Inverted Perovskite Solar Cells. *RSC Adv.* **2017**, *7*, 35819–35826. [CrossRef]
21. Di Giacomo, F.; Castriotta, L.A.; Kosasih, F.U.; Di Girolamo, D.; Ducati, C.; Di Carlo, A. Upscaling Inverted Perovskite Solar Cells: Optimization of Laser Scribing for Highly Efficient Mini-Modules. *Micromachines* **2020**, *11*, 1127. [CrossRef]
22. *IEC 60904–7:2019*; Photovoltaic Devices—Part 7: Computation of the Spectral Mismatch Correction for Measurements of Photovoltaic Devices. BSI Standards Limited: London, UK, 2019; ISBN 978-0-580-97364-2.
23. Mun, H.; Yang, H.; Park, J.; Ju, C.; Char, K. High Electron Mobility in Epitaxial SnO_{2-x} in Semiconducting Regime. *APL Mater.* **2015**, *3*, 076107. [CrossRef]
24. Wang, D.; Muhammad, R.; Hussain, F.; Li, Z.; Graziosi, P.; Neophytou, N. Electron and Hole Mobility of SnO_2 from Full-Band Electron–Phonon and Ionized Impurity Scattering Computations. *Crystals* **2022**, *12*, 1591. [CrossRef]
25. Devižis, A.; Hertel, D.; Meerholz, K.; Gulbinas, V.; Moser, J.E. Time-Independent, High Electron Mobility in Thin PC61BM Films: Relevance to Organic Photovoltaics. *Org. Electron.* **2014**, *15*, 3729–3734. [CrossRef]
26. Mu, H.; Reddy, I.; Hunt, J.; Severs, P.; Patil, S. Electron Mobility Characterization in OLEDs from Ac Small Signal Optical Modulation. *J. Phys. D Appl. Phys.* **2010**, *43*, 195103. [CrossRef]
27. Jiang, Q.; Zhang, L.; Wang, H.; Yang, X.; Meng, J.; Liu, H.; Yin, Z.; Wu, J.; Zhang, X.; You, J. Enhanced Electron Extraction Using SnO_2 for High-Efficiency Planar-Structure $HC(NH_2)_2PbI_3$-Based Perovskite Solar Cells. *Nat. Energy* **2016**, *2*, 16177. [CrossRef]
28. Liu, D.; Wang, G.; Luo, K.; He, X.; Ye, Q.; Liao, C.; Mei, J. Understanding the Role of the Electron-Transport Layer in Highly Efficient Planar Perovskite Solar Cells. *ChemPhysChem* **2017**, *18*, 617–625. [CrossRef]
29. McPherson, J.W. *Reliability Physics and Engineering: Time-to-Failure Modeling*, 3rd ed.; Springer International Publishing: Cham, Switzerland, 2019; ISBN 978-3-319-93682-6.
30. Min, H.; Lee, D.Y.; Kim, J.; Kim, G.; Lee, K.S.; Kim, J.; Paik, M.J.; Kim, Y.K.; Kim, K.S.; Kim, M.G.; et al. Perovskite Solar Cells with Atomically Coherent Interlayers on SnO_2 Electrodes. *Nature* **2021**, *598*, 444–450. [CrossRef]